Quantum transport simulation of nanoscale semiconductor devices based on Wigner Monte Carlo approach

Koba, Shunsuke

Aoyagi, Ryo

Tsuchiya, Hideaki

(Citation)
JOURNAL OF APPLIED PHYSICS,108(6):064504-064504

(Issue Date)
2010-09-15

(Resource Type)
journal article

(Version)
Version of Record

(URL)
https://hdl.handle.net/20.500.14094/90001271

JOURNAL OF APPLIED PHYSICS **108**, 064504 (2010)

Quantum transport simulation of nanoscale semiconductor devices based on Wigner Monte Carlo approach

Shunsuke Koba, Ryō Aoyagi, and Hideaki Tsuchiya[a]
Department of Electrical and Electronics Engineering, Graduate School of Engineering, Kobe University, 1-1 Rokko-dai, Nada-ku, Kobe 657-8501, Japan

(Received 6 July 2010; accepted 6 August 2010; published online 17 September 2010)

In this paper, we present quantum transport simulation of nanoscale semiconductor devices based on Wigner Monte Carlo (WMC) approach. We have found that the WMC approach can accurately handle higher-order quantized subbands, tunneling, quantum reflection, and decoherence processes occurring in nanoscale semiconductor devices. Furthermore, we have demonstrated that carrier quantum transport in source electrode plays an important role in devices extremely downscaled into the nanometer regime. © *2010 American Institute of Physics*. [doi:10.1063/1.3487482]

I. INTRODUCTION

The remarkable advancement in semiconductor microfabrication technology makes the manufacturing of nanoscale devices possible, where nonequilibrium transport and quantum effects directly appear on the device characteristics. To accurately predict the electrical properties of such ultrasmall devices at normal conditions, device simulation must reliably consider both quantum and scattering effects in carrier transport.

The particle-based Monte Carlo (MC) solution of the Boltzmann transport equation (BTE) is acknowledged as a powerful method for accurately describing carrier transport in semiconductor devices within the semiclassical approximation.[1] However, as quantum effects become more and more important with continued downscaling, the semiclassical approach based on the BTE fails to describe the carrier transport accurately. Quantum effects are often incorporated in conventional MC simulation by considering quantum corrections,[2–5] which represent repulsive force from interface and tunneling through potential barrier in terms of "smoothed effective potential," while they keep three-dimensional (3D) description of particles.

On the other hand, most quantum simulations are based on the nonequilibrium Green's function (NEGF) method, which is the most fundamental theoretical model of quantum transport and has been proven to be robust and versatile in ballistic transport simulation.[6] However, in case of incoherent transport with realistic scattering, practical solution of NEGF model requires large computational effort. Therefore, when scattering effects are included, two-dimensional or 3D simulation of actual devices such as metal-oxide-semiconductor field-effect transistor still remains a difficult problem.

Alternatively, the Wigner function formalism seems very appropriate to deal with realistic problems. It is based on the Wigner function defined in the phase-space and allows us a rigorous description of quantum transport.[7] The well-known strong analogy between Wigner and Boltzmann formalisms makes it possible to use similar numerical techniques such as particle MC method by representing the Wigner function as an ensemble of pseudoparticles and by making use of the same scattering probabilities as in the Boltzmann collision operator.[8,9] The major difference between the BTE and the Wigner transport equation (WTE) is the nonlocal potential term of the WTE. While the BTE treats the potential as a localized force term, the WTE treats the potential term nonlocally. Thus, the WTE fully incorporates quantum effects and the nonlocal term causes the Wigner function to take negative values.[10–12]

The negative parts of the Wigner function cannot be accommodated in a normal MC technique. So, in order to account for the negative parts of the Wigner function, introduction of a new property, particle affinity, has been proposed.[8,9] The affinity is a weighting given to each particle to represent its contribution to the total charge distribution of the system. The affinity evolves with time and its magnitude is updated according to the quantum evolution term governed by the nonlocal potential of the WTE. Such a Wigner function-based MC technique is called Wigner MC (WMC) method. The WMC method based on the affinity technique has been proposed by Shifren *et al.*,[8] and lately a fully self-consistent WMC method, in which the handling of the self-consistent Poisson potential and particle injection conditions is revised, has been reported by Querlioz *et al.*[9] In this paper, we apply the approach by Querlioz *et al.* to quantum transport simulation in several nanoscale devices and structures and demonstrate the ability of the fully self-consistent WMC method for studying quantum and dissipative transport of carriers. We further verify that quantum transport in electrode becomes important in devices extremely downscaled into the nanometer regime.

II. WMC APPROACH

The Wigner transport formalism is based on the Wigner function $f_w(x,k)$ defined in the phase-space, and the WTE, the dynamical equation of $f_w(x,k)$, is given by

---

[a] Electronic mail: tsuchiya@eedept.kobe-u.ac.jp.

$$\frac{\partial f_w}{\partial t}+\frac{\hbar k}{m}\frac{\partial f_w}{\partial x}=Qf_w+Cf_w, \tag{1}$$

which is very similar to the BTE. Cf_w represents collision term and if quantum collision effects are neglected and the same collision operator as in the BTE is used, the only difference comes from the term Qf_w, which is the quantum evolution term including the nonlocal effect of the potential and represented by

$$Qf_w(x,k)=-\frac{1}{\hbar}\int_{-\infty}^{\infty}\frac{dk'}{2\pi}V(x,k-k')f_w(x,k'), \tag{2}$$

where the Wigner potential $V(x,k-k')$ is given by using the potential energy distribution $U(x)$ as follows:

$$V(x,k-k')=2\int_0^{\infty}d\xi\,\sin[(k-k')\xi]\times\left[U\left(x+\frac{\xi}{2}\right)-U\left(x-\frac{\xi}{2}\right)\right]. \tag{3}$$

In this study, we will use the same scattering probabilities as in the BTE, which enable us clear comparison between the classical MC and the WMC formalisms. In addition, both the potential barrier and the Poisson potential are considered in $U(x)$ of Eq. (3) in order to incorporate quantum effects not only in quantum regions, but also in external electrodes.[9] Alternatively, the quantum evolution term Qf_w can be represented in powers of $\hbar$ and higher-order spatial derivatives of the potential energy.[7] The $\hbar^2$-order term of them gives a quantum correction of potential[3] or quantum diffusion current[13] with the form of density-gradient.

According to Shifren *et al.*[8] and Querlioz *et al.*,[9] we use the affinity technique to extend the particle MC algorithm to the WTE. In this technique, the Wigner function is defined by the position and the wave vector, and then described as an ensemble of pseudoparticles weighted by the affinity. Hence, the Wigner function takes the form

$$f_w(x,k,t)=\sum_i A_i(t)\delta[x-x_i(t)]\delta[k-k_i(t)], \tag{4}$$

where x_i, k_i, and A_i are the position, the wave vector, and the affinity, respectively, of ith particle. Note that the affinity technique incorporates the wave properties of particles in the simulation. Such quantum particles behave and scatter as classical particles, except that the potential does no longer influence the wave vector but only the affinity through the quantum evolution term $Qf_w(x,k)$. This means that the wave vector can be changed only by scattering. As a result, the equations of motion during a free flight are given by[14–16]

$$\frac{dx_i}{dt}=\frac{\hbar k_i}{m}, \tag{5}$$

$$\frac{dk_i}{dt}=0, \tag{6}$$

$$\sum_{i\in M(x,k)}\frac{dA_i}{dt}=Qf_w(x,k). \tag{7}$$

Note that the affinity of pseudoparticles in a mesh $M(x,k)$ of the phase-space is updated with time according to Eq. (7). This represents that the affinity can take negative values in accordance with the fact that the Wigner function may also be negative. As Querlioz *et al.* pointed out, each mesh of the phase-space must always contain at least one pseudoparticle to ensure the conservation of the total affinity of particles. Therefore, we should inject particles with zero-affinity to every empty mesh where the quantum evolution term is not null. However, by injecting particles to every empty mesh, computational effort drastically increases. To reduce the number of pseudoparticles to be simulated and to ensure the computational accuracy simultaneously, we introduce a criterion for the zero-affinity particle injection as follows:

$$|Qf_w(x,k)|>\frac{0.01}{\Delta t}(\mathrm{s}^{-1}), \tag{8}$$

where, Δt is the time step of the MC simulation. This criterion was derived using the following simple argument. From Eq. (7), the time evolution of the affinities is calculated as

$$A_i(t+\Delta t)-A_i(t)=\frac{1}{n}\Delta t\times Qf_w(x,k,t+\Delta t), \tag{9}$$

where n is the number of pseudoparticles in the mesh $M(x,k)$ of the phase-space. If the right-hand side quantity of Eq. (9) is smaller than 0.01, the difference is negligible since A_i usually takes the value close to 1. In a word, particles with zero-affinity are not necessary to be injected into such a trivial mesh. Consequently, $\Delta t\times|Qf_w(x,k,t+\Delta t)|>0.01n>0.01$ can be used as a guideline whether to inject the zero-affinity particle into empty mesh. We have carefully checked its validity by changing the threshold value and have verified Eq. (8) to work very well. We also add here that a predictor technique of fourth order was adopted to update the pseudoparticle affinities following Eq. (9), which is to make the solution stable.[15,16]

To accurately describe the time evolution of pseudoparticles, discretization scheme for the phase-space must be also stable. Since Eq. (3) is periodic in k-space with a period of $2\pi/\Delta_\xi$, a mesh spacing Δ_ξ for the relative coordinate ξ should be sufficiently small so that π/Δ_ξ must always larger than the maximum k value that carriers can reach. In the WMC method, Δ_ξ can be chosen independently of the real-space mesh spacing Δ_x. On the other hand, k-space meshing determines the number of pseudoparticles and hence the computational time, so its mesh spacing Δ_k with an arbitrary number of mesh points N_k, that is $\Delta_k=2\pi/(N_k\Delta_\xi)$, should be adjusted not to reduce the computational accuracy. Details of other numerical techniques for the fully self-consistent WMC method including boundary conditions are found in.[9,14–17]

Since the WMC technique is a quantum ensemble MC (EMC) based on the full particle nature of the EMC technique, we can utilize ensemble statistics by representing that any ensemble average takes the form

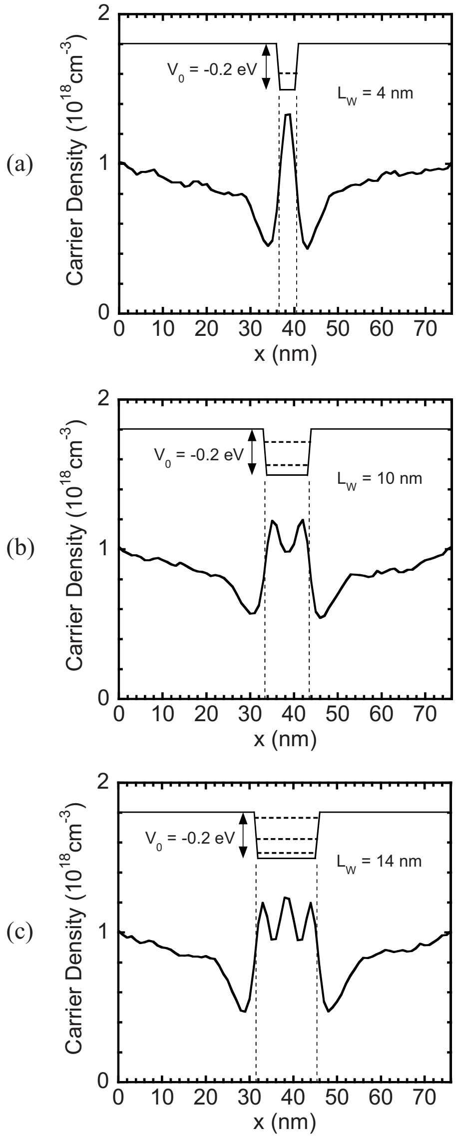

FIG. 1. Electron density distributions computed for single quantum wells with a well width of (a) 4 nm, (b) 10 nm and, (c) 14 nm, where the well depth is assumed to be 0.2 eV. The barrier is AlGaAs doped to 10^{18} cm^{-3} and the well is GaAs slightly doped to 10^{16} cm^{-3}. The Poisson equation is not solved in the simulation.

$$\langle Q\rangle = \frac{\Sigma_i A_i Q_i}{\Sigma_i A_i}, \tag{10}$$

TABLE I. Energy eigenvalues estimated for single quantum wells with three different well widths. They were obtained by numerically solving the Schrödinger equation.

Well width (nm)	E_1 (eV)	E_2 (eV)	E_3 (eV)
4	0.094	⋯	⋯
10	0.031	0.12	⋯
14	0.018	0.073	0.15

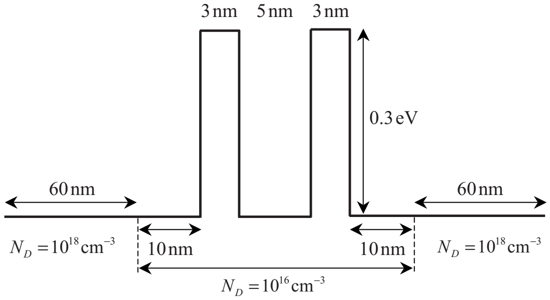

FIG. 2. RTD structure used in the simulation. GaAs quantum well of 5 nm is sandwiched between two AlGaAs barriers of 0.3 eV high and 3 nm wide.

where Q is the quantity of interest such as velocity and energy. The current flowing through the device is calculated by averaging the electron velocities based on the Ramo–Shockley theorem[18] as

$$I(t) = \frac{q}{L}\sum_i A_i(t) v_i(t), \tag{11}$$

where L is the device length.

III. DESCRIPTION OF HIGHER-ORDER QUANTIZED SUBBANDS

Now, we will present the simulated results. First, we examined the ability of the WMC method to describe higher-order quantized subbands by simulating quantum well structures. Figure 1 shows the electron density distributions computed for single quantum wells with a well depth of 0.2 eV and well widths of (a) 4 nm, (b) 10 nm, and (c) 14 nm. The barrier region consists of AlGaAs doped to 10^{18} cm^{-3} and the well region GaAs slightly doped to 10^{16} cm^{-3}. The temperature is 300 K, and the scattering mechanisms considered are optical phonons, elastic acoustic phonons and impurities. In this study, we considered only transport within the Γ valley. It is found that the electron distribution in the quantum well has single-peaked pattern in (a), double-peaked pattern in (b), and triple-peaked pattern in (c), which can easily be assumed due to the change in electron population into higher-order quantized subbands. Here, note that the Poisson's equation was not solved in the calculation, which means that the potential energy profile is frozen to be flat except at the heterojunctions as shown in the insets of Fig. 1. This is because the self-consistent Poisson potential induces band-bending inside the quantum well and drastically modifies electron density profile even when only a single quantized subband exists.

To check the actual number of quantized subbands, we have numerically solved the Schrödinger equation to calculate the energy eigenvalues as shown in Table I. Comparing them to Fig. 1, the number of peaks in the WMC density distributions has proved to be completely consistent with the total number of eigenvalues obtained from the Schrödinger equation. Consequently, the WMC technique is found to be a more accurate quantum tool than quantum-corrected MC techniques, which can represent only the lowest-quantized subband via smoothed effective potential.[2–5]

IV. RESONANT-TUNNELING DIODE

Next, we apply the WMC method to a resonant tunneling diode (RTD), which is one of the appropriate devices to demonstrate the ability of the WMC method to describe

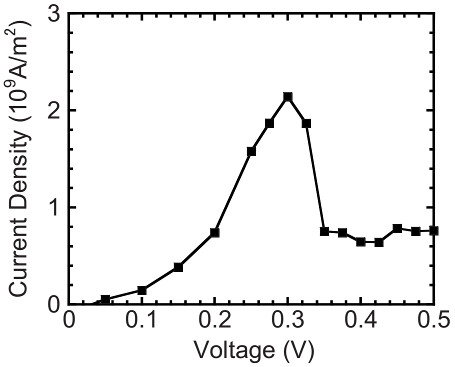

FIG. 3. Computed current-voltage characteristics of RTD.

quantum tunneling and scattering effects. The RTD structure used in the simulation is shown in Fig. 2, where a GaAs quantum well of 5 nm is sandwiched between two AlGaAs barriers of 0.3 eV high and 3 nm wide, which is similar to that computed in.[9] The quantum well, the barriers and 10 nm thick spacer regions adjacent to the barriers are slightly doped to 10^{16} cm^{-3}, while the 60 nm-long access regions are doped to 10^{18} cm^{-3}. As in Sec. III, the temperature is 300 K and the scattering mechanisms considered are optical phonons, elastic acoustic phonons, and impurities, and only the transport within the Γ valley is considered. Here, we should state that the Poisson's equation was self-consistently solved in the present RTD simulation and both the potential barriers and the Poisson potential are treated in the affinity evolution.

The computed current-voltage characteristics are shown in Fig. 3, which correspond well to the result reported in Ref. 9, in terms of peak and valley current densities, and also their occurring bias voltages. In Fig. 4, we plot (a) electron densities and (b) self-consistent potentials for the resonant and the nonresonant biases. On resonance, an obvious peak of electron density is found in the central quantum well, while on nonresonance, an accumulation peak is formed in the left electrode, which is caused by the electrons bounced off the barriers. These results indicate that the WMC method can handle quantum mechanical resonant tunneling accurately.

Next, we examine the ability of handling scattering

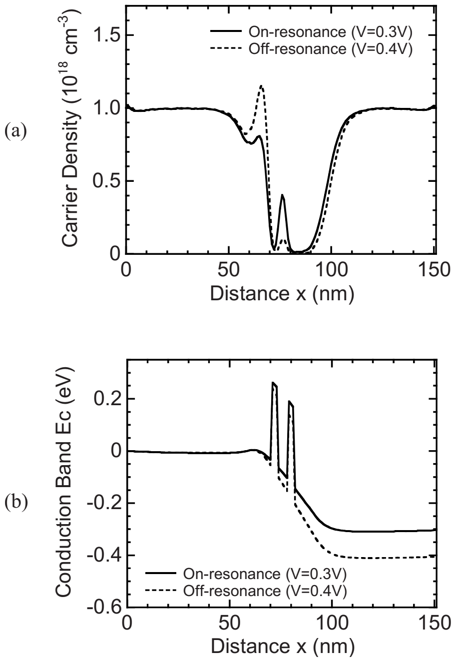

FIG. 4. (a) Electron density and (b) self-consistent potential distributions computed for resonant and nonresonant biases.

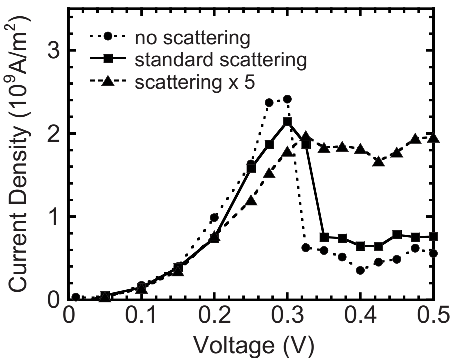

FIG. 5. Influences of scattering on current-voltage characteristics of RTD. Three results computed for no scattering inside the double-barrier region, standard scattering rate and scattering rates multiplied by 5 are plotted.

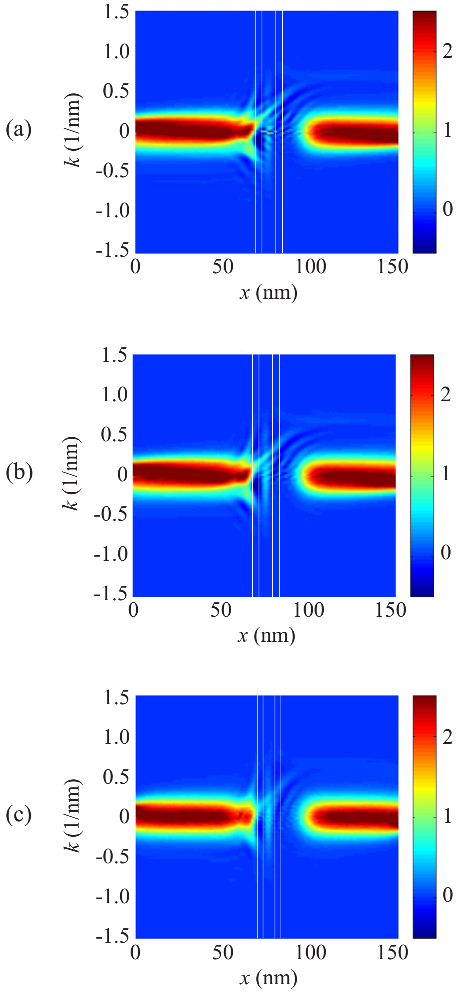

FIG. 6. (Color online) Wigner distribution functions of RTD in the phase-space computed for (a) no scattering inside the double-barrier region, (b) standard scattering rate, and (c) scattering rates multiplied by 5. The bias voltage is all set at $V=0.3$ V.

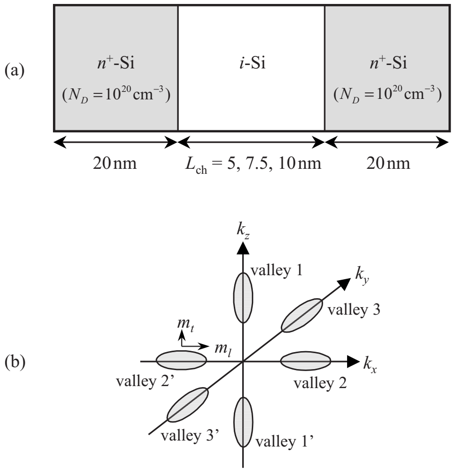

FIG. 7. (a) Device structure of silicon n$^+$-i-n$^+$ diode used in the simulation and (b) conduction band valleys of silicon. The ellipsoidal multivalleys and its band nonparabolicity are taken into account. The channel length L_{ch} is varied from 5 to 10 nm.

effects.[15,19] In Fig. 5, we plot three kinds of current-voltage characteristics computed for no scattering inside the double-barrier region, standard scattering rate and scattering rates multiplied by 5. As expected, the peak current density decreases and the valley current density increases with scattering rates, and thus the peak-to-valley current ratio reduces by scattering. Such decoherence effects due to scattering can also be verified by rendering the Wigner distribution function in the phase-space as shown in Fig. 6, where (a) no scattering inside the double-barrier region, (b) standard scattering rate and, (c) scattering rates multiplied by 5. The bias voltage is all set at $V=0.3$ V. In the right-hand side electrode of Figs. 6(a) and 6(b), we can see the signature of electron waves tunneling through the double-barrier. In addition, a quantum interference pattern inside the central quantum well is clearly visible in Figs. 6(a) and 6(b). On the other hand, such quantum mechanical behaviors almost disappear when the scattering rates are increased by five times as shown in Fig. 6(c). This scattering-induced decoherence tends to degrade the resonant tunneling property as shown in Fig. 5, by increasing the valley current to a current level such that the negative resistance becomes almost unobservable.

As for computational efforts, a large number of simulated particles, i.e., typically between 65,000 and 110,000 depending on bias voltage, are required. The computational time also increases by a factor of about two when compared with the classical MC simulation. Even so, the WMC technique has the ability to handle all quantum effects such as resonant tunneling and higher-order quantization, not to mention all relevant scattering mechanisms as in the standard MC procedure can be handled.

V. SILICON N-I-N DIODE

Finally, we present quantum transport simulation of a silicon device based on the WMC technique. Figure 7 shows (a) the device structure of silicon n$^+$-i-n$^+$ diode used in this study and (b) the conduction band valleys of silicon. It is well-known that silicon has six equivalent ellipsoidal multivalleys near the X point of the first Brillouin zone as shown in Fig. 7(b), so we need to define the Wigner function for each valley, and inject at least one pseudoparticle in each mesh of the six phase-spaces. Therefore, approximately six times larger number of simulated particles than in the RTD simulation is required.[14] In the following simulations, the temperature is 300 K, and the scattering mechanisms considered are intravalley elastic acoustic phonon and intervalley inelastic phonons including f- and g-phonons and impurity scatterings.[1] Here, we emphasize that all of the simulated results are compared with those of the classic MC approach based on BTE, to clarify the quantitative influence of quantum effects.

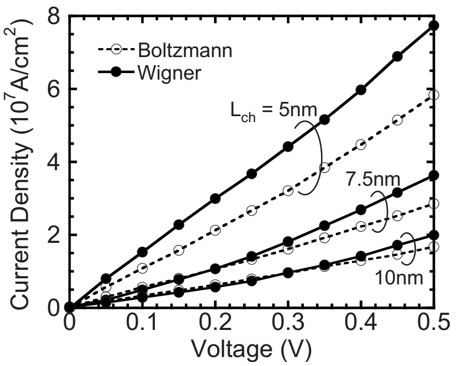

FIG. 8. Current-voltage characteristics of silicon n$^+$-i-n$^+$ diode computed by using Boltzmann and WMC methods. The channel length is 10, 7.5, and 5 nm.

Figure 8 shows the current-voltage characteristics computed for three channel lengths. It is found that the Wigner approach provides very close results to the Boltzmann approach for $L_{ch}=10$ and 7.5 nm, while it gives significantly larger current for $L_{ch}=5$ nm. To understand such behaviors of quantum current-voltage characteristics, we first plot the microscopic quantum features for $L_{ch}=10$ nm in Fig. 9. It is found that the quantum carrier distribution (Wigner) increases in the channel due to tunneling effect as shown in Fig. 9(b), and as a result, the channel potential is elevated due to space charge effect induced by the increased electron

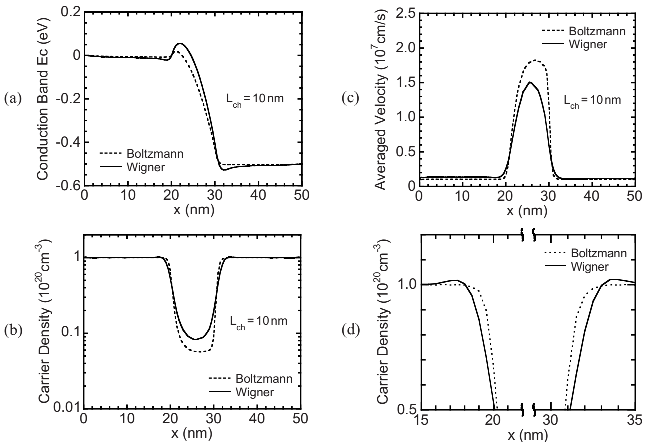

FIG. 9. (a) Potential energy, (b) carrier density, and (c) averaged carrier velocity distributions computed at $V=0.5$ V. $L_{ch}=10$ nm. (d) represents the magnified carrier density distributions around the source/channel and channel/drain junctions.

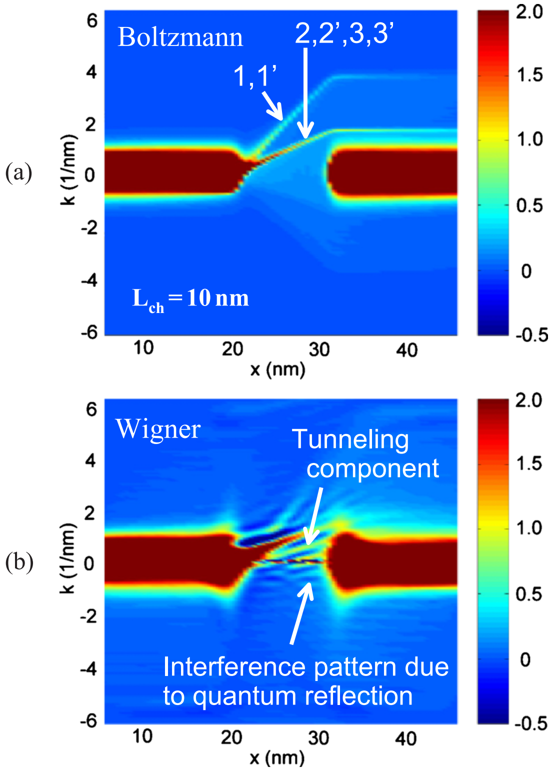

FIG. 10. (Color online) Distribution functions in phase-space computed by using (a) Boltzmann and (b) WMC methods. $V=0.5$ V and $L_{ch}=10$ nm. Numbers 1, 1′, 2, 2′, 3, and 3′ in (a) correspond to the valley numbers in Fig. 7(b). Due to the interference pattern, the distribution function appears inseparable into each valley in (b).

density as shown in Fig. 9(a). Contrary to the channel electrostatics, the potential in electrodes slightly descends in the close vicinity of the channel. As clearly indicated in Fig. 9(d), this is due to the expansion of carrier depletion region caused by nonlocal quantum repulsive force from the channel potential barrier. Furthermore, as shown in Fig. 9(c) the averaged carrier velocity decreases in the channel as compared with the Boltzmann approach, which is due to the fact that thermally injected electrons have smaller kinetic energy because of the formation of higher potential barrier [Fig. 9(a)] and that tunneling electrons travel more slowly than the thermally injected ones. It is also worth noting that the averaged velocity drastically reduces in the second half of the channel, which is possibly due to quantum reflection effect appearing in ballistic transport.[16,20] Indeed, by comparing the Boltzmann and Wigner distribution functions as plotted in Fig. 10, interference pattern is observed in the Wigner result, which is the signature of ballistic transport with quantum reflection. It is interesting that the significant differences between the Boltzmann and Wigner approaches observed at the microscopic level are almost reduced at the macroscopic level in terms of terminal current, which is the same as in the case of carbon nanotube field-effect transistors (FETs) reported in Refs. 16 and 20.

Next, the microscopic quantum features for the shorter $L_{ch}=5$ nm are also examined as shown in Figs. 11 and 12. In this extremely scaled device, the slowdown associated with tunneling and quantum reflection is mitigated. Instead, carrier acceleration occurs in the source region as shown in Figs. 11(c) and 12(b), which is due to the unexpected electric field caused by the nonlocal carrier depletion effect mentioned above. In fact, we have performed classical MC simulations under the frozen potential using the potential profile obtained from the Wigner approach and in consequence the larger current density in the Wigner approach for $L_{ch}=5$ nm is confirmed due both to carrier acceleration in the source region and quantum tunneling effect. The above results indicate that the quantum transport in not only channel region but also source region plays an important role in silicon devices scaled-down to the nanometer regime.

VI. CONCLUSION

We have shown for the first time that the WMC approach can describe higher-order quantized subbands by simulating electron injection processes into single quantum wells. This is one of the advantages over the quantum correction approaches, which can produce spatial carrier distribution of only the lowest-quantized subband via smoothed effective potential. We have also demonstrated that the WMC ap-

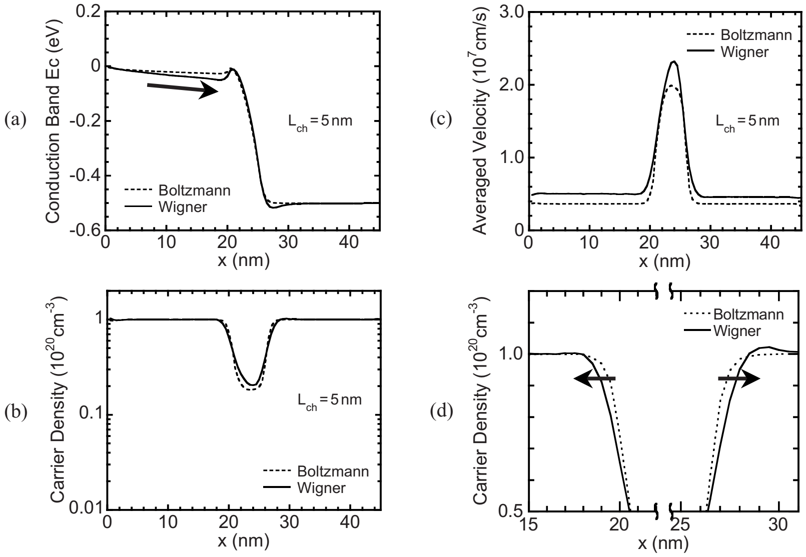

FIG. 11. (a) Potential energy, (b) carrier density, and (c) averaged carrier velocity distributions computed at $V=0.5$ V. $L_{ch}=5$ nm. (d) represents the magnified carrier density distributions.

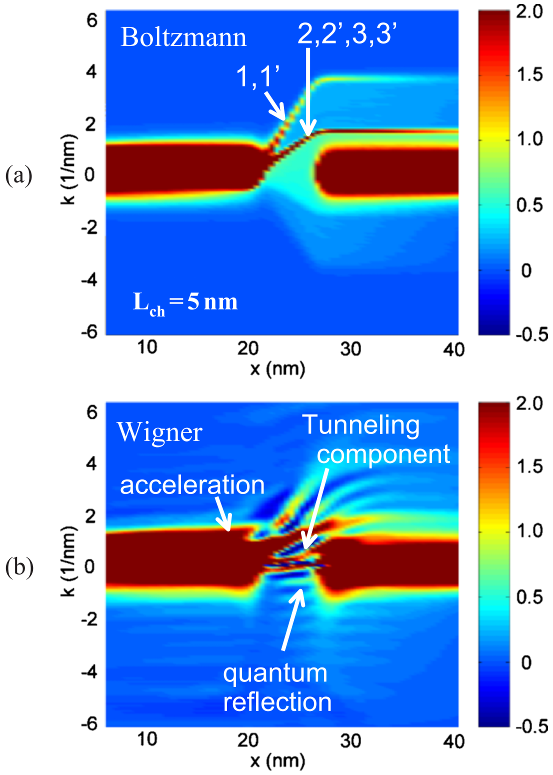

FIG. 12. (Color online) Distribution functions in phase-space computed by using (a) Boltzmann and (b) WMC methods. $V=0.5$ V and $L_{ch}=5$ nm.

proach can quite clearly reveal the tunneling, quantum reflection, and decoherence processes occurring in nanoscale semiconductor devices.

Furthermore, we have found that carrier quantum transport in not only channel region, but also source region plays an important role in silicon devices scaled less than 10 nm. Therefore, a global quantum simulator that can describe both quantum and scattering effects throughout the device is required. From this point of view, the ability of the WMC approach to describe quantum transport between the source and drain electrodes will make a significant contribution in practical design of nanoscale FETs under quasiballistic transport.

ACKNOWLEDGMENTS

This work was supported by the Semiconductor Technology Academic Research Center (STARC).

[1] C. Jacoboni and L. Reggiani, Rev. Mod. Phys. **55**, 645 (1983).
[2] D. Ferry, R. Akis, and D. Vasileska, Tech. Dig. - Int. Electron Devices Meet. **2000**, 287.
[3] H. Tsuchiya, M. Horino, M. Ogawa, and T. Miyoshi, Jpn. J. Appl. Phys., Part 1 **42**, 7238 (2003).
[4] B. Winstead and U. Ravaioli, IEEE Trans. Electron Devices **50**, 440 (2003).
[5] B. Wu, T.-W Tang, J. Nam, and J.-H. Tsai, IEEE Trans. Nanotechnol. **2**, 291 (2003).
[6] S. Datta, *Electronic Transport in Mesoscopic Systems* (Cambridge University Press, Cambridge, U. K., 1995).
[7] E. Wigner, Phys. Rev. **40**, 749 (1932).
[8] L. Shifren, C. Ringhofer, and D. Ferry, IEEE Trans. Electron Devices **50**, 769 (2003).
[9] D. Querlioz, P. Dollfus, V.-N. Do, A. Bournel, and V. Nguyen, J. Comput. Electron. **5**, 443 (2006).
[10] W. Frensley, Phys. Rev. B **36**, 1570 (1987).
[11] N. Kluksdahl, A. Kriman, D. Ferry, and C. Ringhofer, Phys. Rev. B **39**, 7720 (1989).
[12] H. Tsuchiya, M. Ogawa, and T. Miyoshi, IEEE Trans. Electron Devices **38**, 1246 (1991).
[13] M. Ancona and G. Iafrate, Phys. Rev. B **39**, 9536 (1989).
[14] D. Querlioz, J. Martin, K. Huet, A. Bournel, V. Fortuna, C. Chassat, S. Retailleau, and P. Dollfus, IEEE Trans. Electron Devices **54**, 2232 (2007).
[15] D. Querlioz, H.-N. Nguyen, J. Martin, A. Bournel, S. Retailleau, and P. Dollfus, J. Comput. Electron. **8**, 324 (2009).
[16] D. Querlioz and P. Dollfus, *The Wigner Monte Carlo Method for Nanoelectronic Devices* (Wiley, New York, 2010).
[17] D. Querlioz, J. Martin, V.-N. Do, A. Bournel, and P. Dollfus, IEEE Trans. Nanotechnol. **5**, 737 (2006).
[18] H. Kim, H. Min, T. Tang, and Y. Park, Solid-State Electron. **34**, 1251 (1991).
[19] D. Querlioz, J. Martin, A. Bournel, and P. Dollfus, Phys. Rev. B **78**, 165306 (2008).
[20] H.-N. Nguyen, D. Querlioz, S. Retailleau, A. Bournel, and P. Dollfus, Proceedings of the 13th International Workshop on Computational Electronics, Beijing, May 27-29, 2009, p. 257.